

Combinatorial Effect of Various Features Extraction on Computer Aided Detection of Pulmonary Nodules in X-ray CT Images

NORIYASU HOMMA
Graduate School of Medicine
Tohoku University
2-1 Seiryomachi, Aoba-ku
Sendai 980-8575
JAPAN
homma@ieee.org
<http://homma.shs.tohoku.ac.jp>

KAZUNORI TAKEI
Business Group
TIS Inc.
Kaigan 1, Minato-ku
Tokyo 105-8624
JAPAN
ktakei@tis.co.jp

TADASHI ISHIBASHI
Graduate School of Medicine
Tohoku University
2-1 Seiryomachi, Aoba-ku
Sendai 980-8575
JAPAN
tisibasi@mail.tains.tohoku.ac.jp

Abstract: In this paper, we propose a new method for computer aided detection of pulmonary nodules in X-ray CT images to reduce false positive rate under high true positive rate conditions. An essential part of the method is to extract and combine two novel and effective features from the original CT images: One is orientation features of nodules in a region of interest (ROI) extracted by a Gabor filter, while the other is variation of CT values of the ROI in the direction along body axis. By using the extracted features, pattern recognition techniques can then be used to discriminate between nodule and non-nodule images. Simulation results show that discrimination performance using the proposed features is extremely improved compared to that of the conventional method.

Key-Words: Computer aided diagnosis, Lung cancer, Pulmonary nodules, Feature extraction, Image recognition, X-ray CT images

1 Introduction

With the increasing mortality rate for lung cancer, X-ray computed tomography (CT) has been used for detection of lung cancer at early stages [1]. The early stage detection of lung cancer is extremely important for survival rate and this is true for any pathological cells of lung cancer [2]. Using the X-ray CT, pulmonary nodules that are typical shadows of pathological changes of lung cancer [3] can be detected more clearly compared to the chest X-ray examination even if they are at early stages. This is an advantage of the X-ray CT diagnosis. In fact, it has been reported that the survival rate of the later ten years can reach 90% after the detection at early stages using X-ray CT images [4].

On the other hand, using the X-ray CT may exhaust radiologists because the CT generates a large number of images (at least over 30 images per patient) and they must diagnose all of them. The radiologists' exhaustion and physical tiredness might cause a wrong diagnosis especially for a group medical examination where most of CT images are healthy and only very few images involve the pathological changes. Therefore, some computer-aided diagnosis (CAD) systems have been developed to help their diagnosis work [5, 6]. Although these CAD systems can automatically detect pulmonary nodules with a high true positive rate (TP), the false positive rate (FP)

is also high. To reduce the FP, several advanced methods such as neural network approaches have been proposed [7, 8]. However, there are still some fundamental problems such as a low discrimination rate for variations of size and positional shift of nodule images. This is because they are still so-called low level or simple image recognition methods with pixel based features compared to the radiologist's complex diagnosis process.

In this paper, to further reduce the FP, we propose new methods to extract and combine novel features from the CT images of pulmonary nodules. The extraction and combination of new features are motivated by the radiologist's higher level cognitive process in which several features are combined and integrated to conduct precise diagnosis. Simulation results demonstrate the effectiveness of the new features and the combination method for discriminating nodule shadows from non-nodule ones.

2 Method

In general, a discrimination method mainly consists of the feature extraction and pattern recognition techniques. The conventional image features are such as average, variance, and entropy of pixel values [9]. However, they are not very effective and don't directly reflect target shapes in CT images that are one of the most important pieces of information used

to discriminate between nodules and non-nodules. Therefore, the proposed method in this paper first pays attention to extracting a new shape feature that is more effective than conventional ones.

2.1 Detection of Regions of Interest (ROI)

First, we use the variable N-quoit filter [5], based on a mathematical morphological technique [10], to detect regions of interest (ROI) from the original CT images. Let us consider an original image $I(x, y)$ of the pixel values at position (x, y) . To apply the N-quoit filter to the image I , we define two elemental functions, D with a disk domain K_D and R with a ring domain K_R , as follows [11].

$$D(x_1, y_1) = \begin{cases} 0 & (x_1, y_1) \in K_D \\ -\infty & \text{otherwise} \end{cases} \quad (1)$$

$$R(x_1, y_1) = \begin{cases} 0 & (x_1, y_1) \in K_R \\ -\infty & \text{otherwise} \end{cases} \quad (2)$$

where

$$K_D = \{(x_1, y_1) \mid x_1^2 + y_1^2 \leq r_1^2\} \quad (3)$$

$$K_R = \{(x_1, y_1) \mid r_2^2 \leq x_1^2 + y_1^2 \leq r_3^2\} \quad (4)$$

r_1, r_2 , and r_3 are radii of the disk, internal, and external rings, respectively. Usually, $r_1 = r_3$ and $r_2 < r_3$.

The output of the N-quoit filter, q , is calculated as

$$q(x, y) = h_D(x, y) - h_R(x, y) \quad (5)$$

where h_D and h_R can be defined by using the operator \oplus of the Minkowsky's set addition [10]

$$\begin{aligned} h_D(x, y) &= I(x, y) \oplus D(x_1, y_1) \\ &= \max_{(x_1, y_1) \in K_D} \{I(x - x_1, y - y_1) \\ &\quad + D(x_1, y_1)\} \end{aligned} \quad (6)$$

$$\begin{aligned} h_D(x, y) &= I(x, y) \oplus R(x_1, y_1) \\ &= \max_{(x_1, y_1) \in K_R} \{I(x - x_1, y - y_1) \\ &\quad + R(x_1, y_1)\} \end{aligned} \quad (7)$$

Using the disk and ring functions, the output $q(x, y)$ results in large for island shadows in the image I , otherwise $q(x, y)$ becomes small. Since the pulmonary nodules often look like small islands in the CT slice images, the filter can effectively detect regions including nodule candidates with high q values.

2.2 Orientation features extraction

To extract features for nodules recognition, we binarize the original images I in the ROI as

$$I_\beta(x, y) = \begin{cases} 1, & I(x, y) \geq \text{mean}(I) + \beta \\ 0, & \text{otherwise} \end{cases} \quad (8)$$

and calculate three conventional features (mean, variance, and entropy of pixels intensity) of the binarized image I_β [12].

Then, we apply a Gabor filter to the binarized image I_β and extract M orientation outputs. The impulse response of the filter is defined by the harmonic function multiplied by the Gaussian function

$$g(x, y, \sigma, \lambda, \gamma, \theta) = \exp\left(-\frac{x'^2 + \gamma^2 y'^2}{2\sigma^2}\right) \times \cos\left(2\pi \frac{x'}{\lambda}\right) \quad (9)$$

where θ is the angle of orientation, σ is the bandwidth, γ is the aspect ratio, and λ is the wave length, respectively. x' and y' are given by

$$\begin{cases} x' = x \cos \theta + y \sin \theta \\ y' = -x \sin \theta + y \cos \theta \end{cases} \quad (10)$$

Orientation features are obtained from the convolution of image $I_\beta(x, y)$ and $g(x, y, \sigma, \lambda, \gamma, \theta)$ as

$$O(x, y) = I_\beta(x, y) * g(x, y, \sigma, \lambda, \gamma, \theta) \quad (11)$$

Fig. 1 shows examples of filtered images of four orientations. Using the new orientation features, the circle-like shadows can be discriminated from the other shapes. This is a promising result because nodule shadows often look like circles. The orientation features involving such circle-shape information can thus be appropriate for the discrimination.

For each orientation, we calculate the three features of mean, variance, and entropy of intensity. Consequently, we extract a total $3 \times (M + 1)$ features from the binarized image. Then we define a vector X of $3 \times (M + 1)$ features, $X = [x_1, x_2, \dots, x_{3(M+1)}]^T$, for the image in ROI. To eliminate the dimensional redundancy of the vector, we finally define a feature vector X' from the vector X by using the principal component analysis technique.

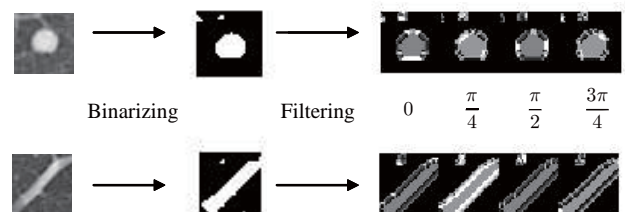


Figure 1: Examples of four orientation filtered outputs.

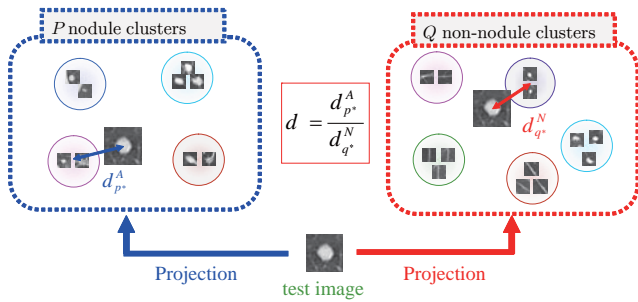


Figure 2: Distances from the test image to centers of P nodule and Q non-nodule clusters.

2.3 Pattern classification in principal component space

We make, respectively, P and Q clusters of nodules and non-nodules images of training data on the principal component feature space by K -means method. The numbers of nodule and non-nodule clusters, P and Q , can be determined automatically on the basis of variance equalization between clusters [13]. Then, we project test data X' into the feature space and calculate Euclidean distances between test data and all the cluster centers (Fig. 2). Here any other distances such as the inner product and Maharanobis distance can be used as the similarity measure, but if the variances are almost the same among clusters, then Maharanobis distance are equivalent to Euclidean distance.

Let us consider the $(P + Q)$ distances d_p^A , $p = 1, 2, \dots, P$, from the P nodule clusters and d_q^N , $q = 1, 2, \dots, Q$, from the Q non-nodule ones. The discrimination is conducted by comparing the minimum distances $d_{p^*}^A$, $p^* \in \{1, 2, \dots, P\}$, from the nearest nodule cluster and $d_{q^*}^N$, $q^* \in \{1, 2, \dots, Q\}$, from the non-nodule one. That is, if the ratio

$$d = \frac{d_{p^*}^A}{d_{q^*}^N} \quad (12)$$

is less than a threshold α , then the test image can be a nodule candidate; otherwise it is a non-nodule candidate.

2.4 Effect of orientation feature

To evaluate the effect of the orientation feature on the discrimination between nodule and non-nodule images, we have tested the proposed method by using a data set from the Web database of CT images [14].

We used a set of 297 nodule data images (208 training and 89 test images) and 1929 non-nodule data images (1351 training and 578 test images). The ROI size was 33×33 pixels and the binarizing threshold β was 40. The number of orientations M was 4 and the

Gabor filter's parameters λ , σ , and γ were 1.5, 2.6, and 1, respectively. The number of principal components C was 5, defined as the minimum number that satisfies $\sum_{j=1}^C u_j > 0.95$ where u_j is the contribution ratio of principal component j . The number of clusters was 35 (25 nodules and 10 non-nodules).

2.4.1 Clustering results

Figs. 3 - 7 show sample images of feature vectors belonging to clusters made from training nodule images. The results demonstrate that each cluster consists of similar circle-like shapes of nodules. This suggests

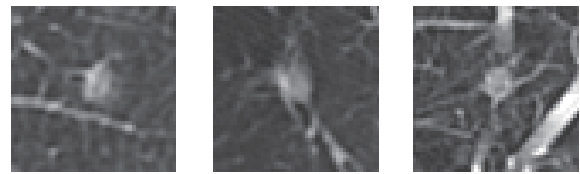


Figure 3: Nodule images in cluster A. Images including relatively light and fuzzy boundary shadows are involved in this cluster.



Figure 4: Nodule images in cluster B. Images including relatively bright, smooth boundary and large circle shadows are involved in this cluster.



Figure 5: Nodule images in cluster C. Images including smooth boundary and small circle shadows are involved in this cluster.



Figure 6: Nodule images in cluster D. Images including small circle with spiculated boundary shadows are involved in this cluster.

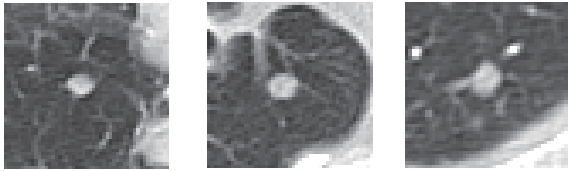


Figure 7: Nodule images in cluster E. Images including ellipse shadows are involved in this cluster.

that the orientation features extracted from the nodule images can be useful for clustering them, and thus the proposed feature is effective for nodule discrimination.

On the other hand, Figs. 8 - 13 show sample images of feature vectors belonging to non-nodule clusters. The results demonstrate that some clusters are composed of similar shapes of non-nodules, but some are not. For example, in cluster nA, most of images look like small circles, but there are a few images not involving such small circle shapes. Also, there are

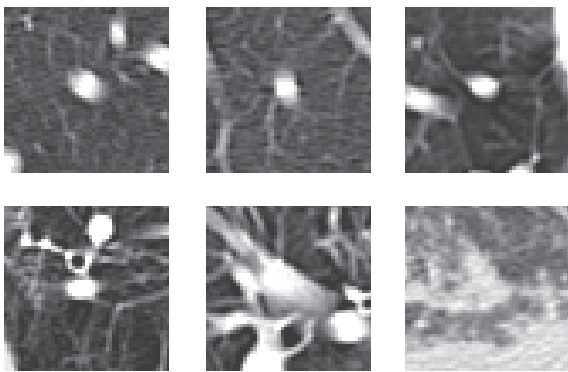


Figure 8: Non-nodule images in cluster nA. Images including relatively small circle shadows are involved in this cluster.

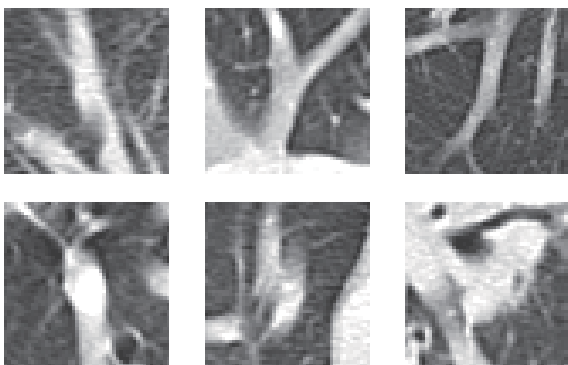


Figure 9: Non-nodule images in cluster nB. Images including vertical line segments are involved in this cluster.

no similar shapes with each other in cluster nF. This implies that non-nodule clusters are composed of various images with relatively high variance of feature vectors, compared to similar images with low variance of feature vectors in nodule clusters. Indeed, variances of feature vectors in non-nodule clusters are

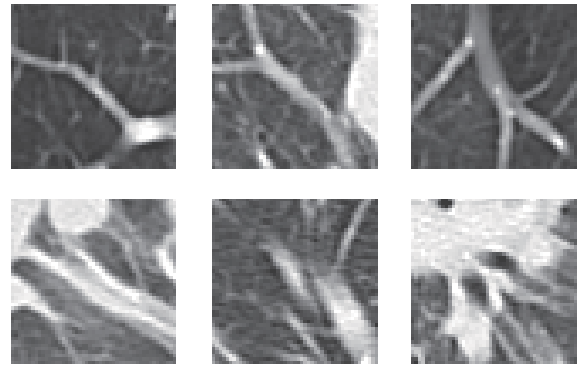


Figure 10: Non-nodule images in cluster nC. Images including line segments with angle $-\pi/4$ [rad] are involved in this cluster.

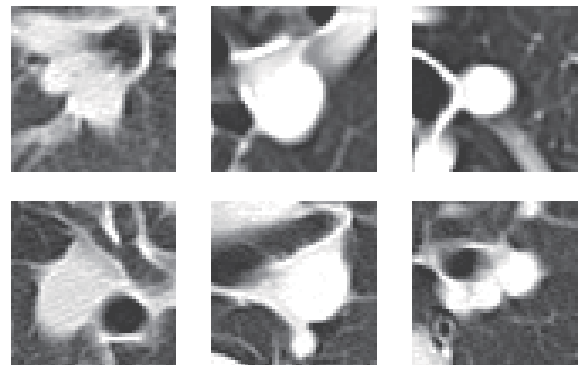


Figure 11: Non-nodule images in cluster nD. Images including relatively large circle shadows are involved in this cluster.

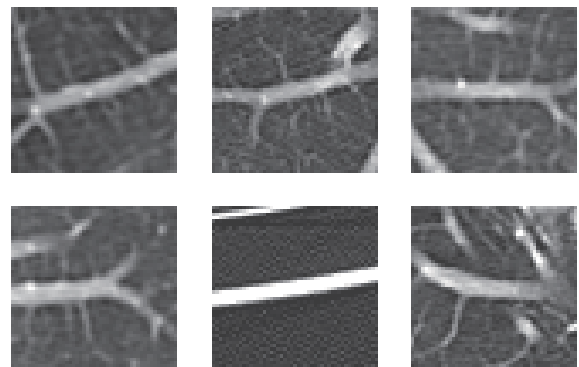


Figure 12: Non-nodule images in cluster nE. Images including horizontal line segments are involved in this cluster.

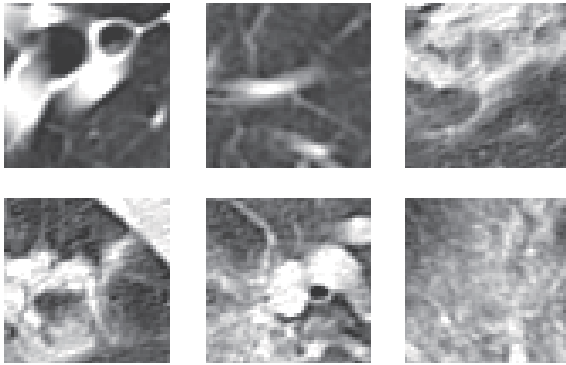


Figure 13: Non-nodule images in cluster nF. Various shapes are involved in this cluster.

relatively high, while variances in nodule clusters are relatively low. The averages of the variances in non-nodule and nodule clusters were 0.003 and 0.001, respectively.

This suggests that further improvement for non-nodule clustering can be done by extracting more effective features from the original images. Such improvement will be discussed in section 3.1.

2.4.2 ROC analysis

Fig. 14 shows the 3 receiver operating characteristic (ROC) curves. Without 12 features of 4 orientations extracted by the Gabor filter, FP was about 80% when TP was 80%, while FP was about 35% by using the orientation features. The improvement of the discrimination rate (FP was improved from 80% to 35%) clearly demonstrates the effectiveness of the proposed feature on the diagnosis of pulmonary nodules.

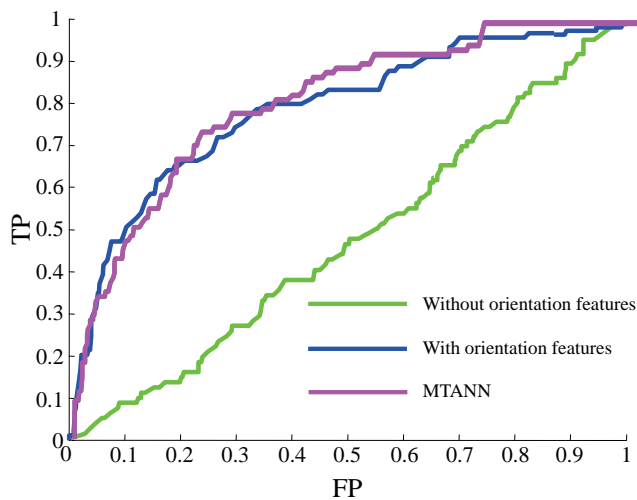


Figure 14: ROC curves.

On the other hand, FP was about 30% under the same condition by using a massive training artificial neural network (MTANN) [7]. Although these rate can be improved if we could choose more suitable settings for both the proposed and MTANN methods, we may claim that the discrimination performances of both methods are almost equivalent.

2.5 Variation feature along body axis

To further improve the discrimination rate for clinical use, we will now try to extract another effective feature. To begin with, let us consider why the discrimination performance using the orientation feature is not enough and what kind of images can be misjudged. For example, Fig. 15 shows a CT slice image of a patient. As mentioned in section 2.2, nodules often have circle-like shadows and thus we want to extract such shape information by using the Gabor filter. It seems, however, hard to discriminate between nodule and non-nodule images, for example nodule images in cluster C (Fig. 5) and non-nodule images in cluster nA (Fig. 8), by using only such shape feature although the proposed one can be more effective than some conventional ones as demonstrated in the preceding section.

Different from the shape information within a CT slice, a novel feature can be extracted from shadow shapes across CT slices in the direction along the body axis. For example, Figs. 16 and 17 are CT slices above and below Fig. 15. Note that, according to a common opinion of several radiologists, circle-like shapes of non-nodules are almost shadows of blood

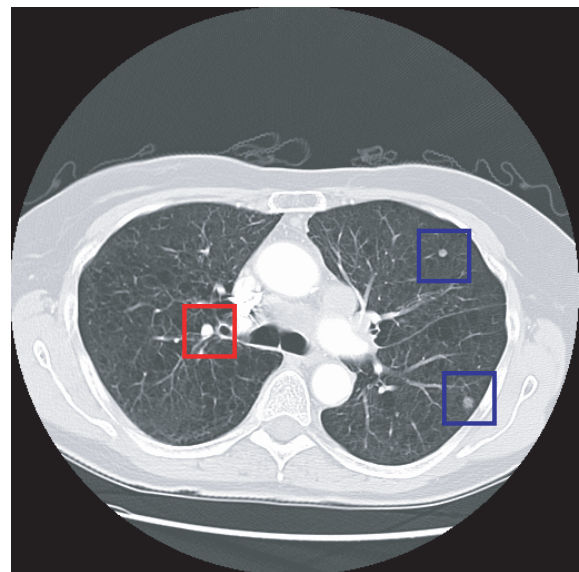


Figure 15: ROI images detected by the variable N-quoit filter. Blue frames indicate images including nodules, whereas the red frame indicates a non-nodule image.

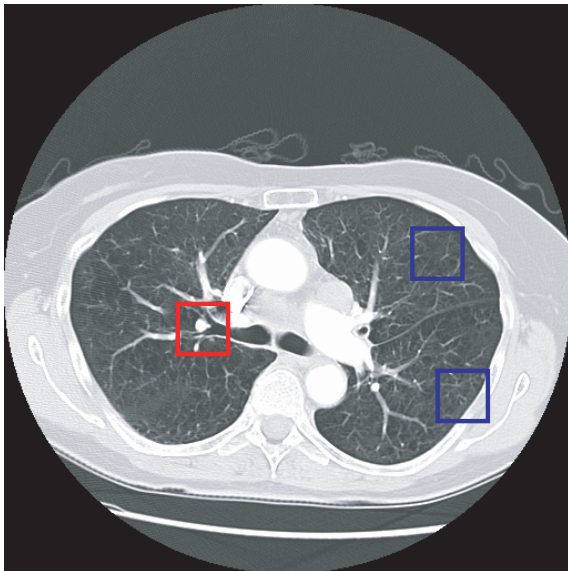


Figure 16: CT slice image above the slice of Fig. 15. The red frame shows continuity between Figs. 15 and 16, in which a circle-like shadow remains at the same position in both figures. On the other hand, the blue frames show discontinuity that sizes and CT values of circle-like shadows in both figures are different from each other.

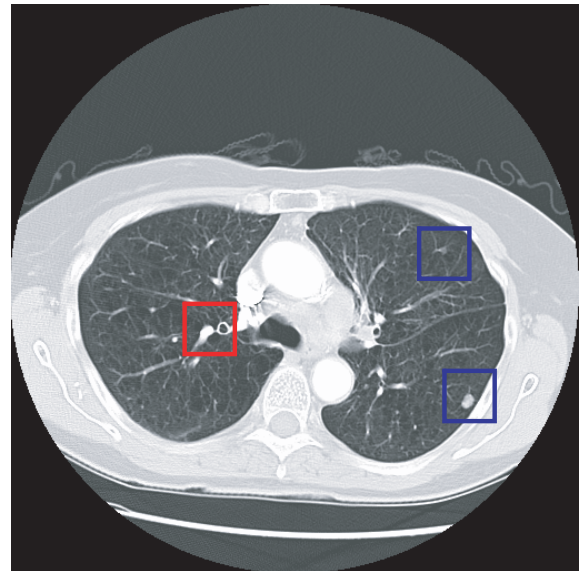


Figure 17: CT slice image below the slice of Fig. 15. As same in Fig. 16, we can see continuity of a non-nodule shadow and discontinuity of nodule shadows.

vessels in the direction along the body axis. In this case, as seen in these figures, the blood vessels are cylinder-like shapes and thus the circle-like shadows remain at the same position if we look at slices above and below the target slice. On the other hand, nodules are often ball shapes. In this case, if we look at a slice above or below the target slice, the circle-like shadows often disappear. Thus, as a new feature, we employ the variation of CT values in the direction along body axis.

To extract the variation feature, we first calculate the average pixel value of the shadow image in the ROI. If a shadow is of a non-nodule and a part of the cylinder-shape blood vessels along the body axis, continuity of the average values can be observed. On the other hand, if the shadow is of a nodule, then discontinuity of the average can be observed. In other words, for the non-nodule case, the average value is almost the same in above and below slices, while the average changes depended on the slices for the nodule case.

Let us denote the average values of the shadows V_m , V_u , and V_l for the target slice, and slices above and below the target, respectively. Using the averages, we define a new feature of shadow variation in the direction along the body axis T by

$$T = \max(T_u, T_l) \quad (13)$$

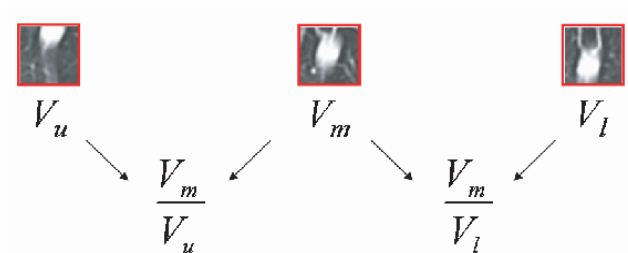


Figure 18: Extraction of the shadow variation feature T .

where

$$T_u = |1 - V_m/V_u| \quad (14)$$

$$T_l = |1 - V_m/V_l| \quad (15)$$

The concept of calculation of the feature extraction is illustrated in Fig. 18.

The new feature T tends to be small for non-nodule shadows of the continuity case while it is large for nodule shadows of the discontinuity case. In fact, for the data used in section 2.4, the average value of the variation T for non-nodule images was 0.182, while the average of T was 0.479 for nodules.

3 Results and discussions

Here the shadow variation feature T was first applied to the ROI images and then more careful discrimination using the orientation features was conducted. That is, if the variation feature T of a candidate shadow in a ROI is less than a threshold T_h ,

the proposed method regards the shadow as a non-nodule. Otherwise, if $T \geq T_h$, the candidate shadow in the ROI is discriminated by using the orientation features as described in section 2.3. It might be worth mentioning an interesting fact that radiologists first detect ROIs of candidate shadows from the original CT slices by using such variation information along the body axis, and then diagnose the detected ROIs by using more detailed information such as shape, size, and CT values of shadows. This is the reason why we use the variation feature T before the orientation ones.

We have evaluated the effect of the new features on the discrimination rate by using the ROC analysis. Fig. 19 shows ROC curves by the conventional method and proposed methods without and with the variation feature T . By using the variation feature, FP was about 20% when TP was 90% in the case of the threshold $T_h = 0.206$. On the other hand, FP was beyond 50% without the feature T . In other words, the discrimination rate FP was improved from about 50% to 20% under the condition TP=90%. Note that the condition TP=90% is good enough for clinical applications of pulmonary nodules diagnosis. Thus, the improvement clearly demonstrates usefulness of the variation feature.

The fact that TP does not reach 100% in Fig. 19 might be a disadvantage of the proposed method with the variation T . This is because a few nodule shadows were regarded as non-nodule shadows by the variation threshold. As a second opinion for clinical use, however, robustness of the performance for various conditions is more important than TP=100% (TP \geq 90% is often good enough). Indeed, the performance is robust for various threshold values and thus it can be another advantage for clinical use.

In addition to this, as shown in Fig. 14, perfor-

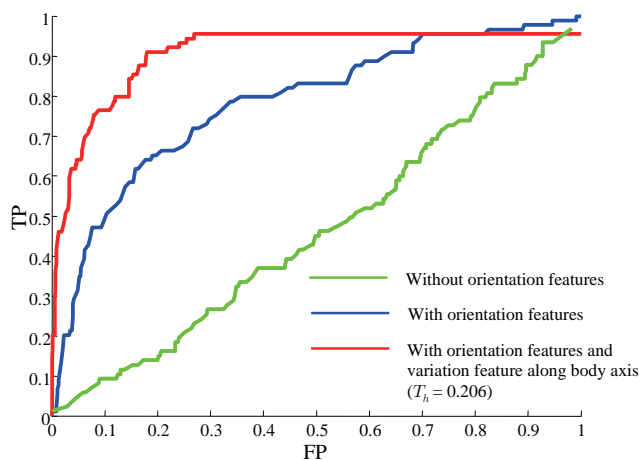


Figure 19: ROC curves.

mance of MTANN[7] was almost the same as that of the proposed method without the variation feature. Consequently, performance of the proposed method with the variation feature can be superior to that of the MTANN.

Finally, similar information to the variation T can be obtained by 3-dimensional images reconstructed from helical CT data [11]. However, calculation of the variation T is very simple and thus less computationally expensive.

3.1 Toward further improvement

3.1.1 A new feature of circle-like shapes

Fig. 20 shows examples of the true positive and false positive images under the condition TP=90% and FP=20%. It seems that the TP and FP images can further be distinguished by their shapes: TP images are circle-like shapes while FP images are tree branch-like shapes of blood vessels or more complex shapes. The proposed orientation features do not work well for these images, although they are very effective for the greater part of images as described above.

As discussed in section 2.4.1, nodule images are clustered well compared to non-nodule images clustering. A wide non-nodule cluster region with high variances can affect the FP results because the distance to the FP image may be overestimated even if an image involved in a non-nodule cluster is close to the FP image in the feature vector space.

Another reason for this may be that the features are calculated for each orientation independently, but their relation among the orientations is not considered at least explicitly. For example, as illustrated in Fig.

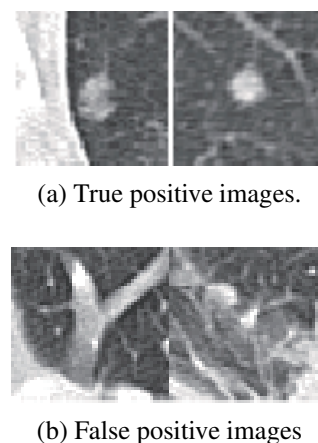


Figure 20: Examples of the true positive and false positive images. True positive means that the discrimination result of the CAD system is nodule and it is really nodule whereas the false positive means that the system's result is nodule, but it is non-nodule.

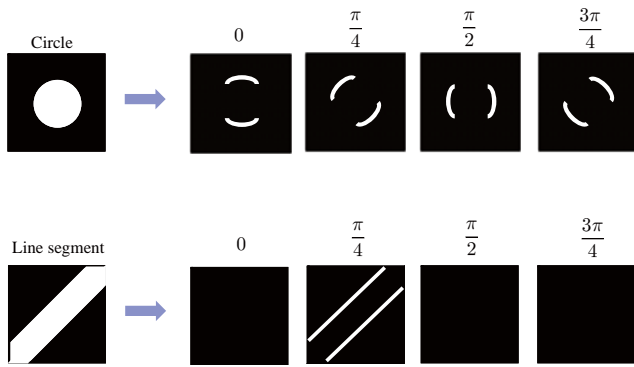


Figure 21: Expected relation between different angles for circle-like and tree branch-like shapes.

21, we can expect that average pixel values extracted by the Gabor filter for all orientations are almost the same for circle-like shapes, while the averages are different from each other for line segments or tree branch shapes.

To extract such differences between orientations, higher angle resolution may be necessary. However, as shown in Fig. 22, the discrete Gabor filter function is depended on the angle because of the small size of ROI. In such case, the sums of pixel values extracted the Gabor filter are different from each other even for the circle-like shapes.

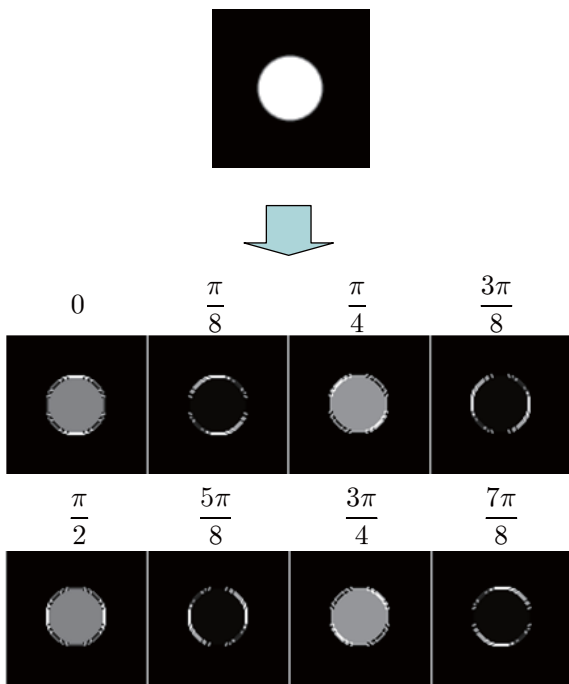
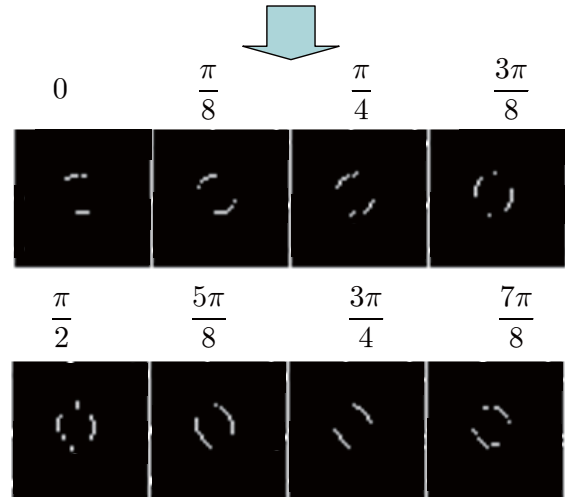
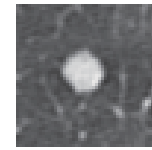


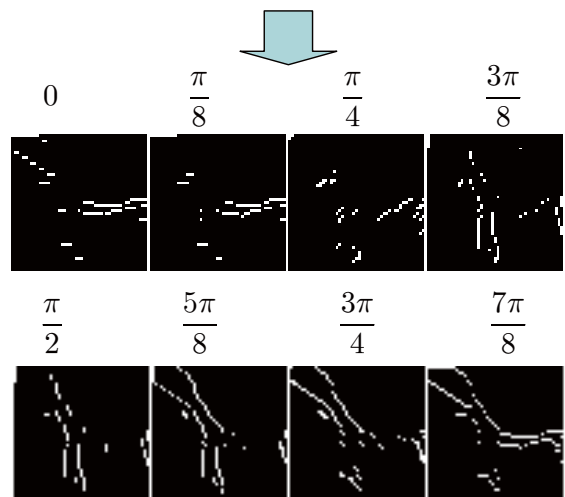
Figure 22: Angle dependency of the Gabor filter outputs: Extracted values of inner and edge pixels are different from each other for various angles.

nodule image



(a) Improved Gabor filter output for a circle-like shape.

non-nodule image



(b) Improved Gabor filter output for a tree branch-like shape.

Figure 23: Extracted values of inner and edge pixels are (a) almost the same for a circle-like shape, but (b) different from each other for a tree branch-like shape.

To overcome this problem, we conducted an edge detection technique as preprocessing the original images, and then the output images of the Gabor filter were binarized to eliminate the error caused by the spatial resolution. By this improvement, as shown in Fig. 23, average values of $M = 8$ orientations can be almost the same for all orientations for the circle-like shape, while for the branch-like shapes, the 8 average values are different from each other depending on the orientation of the branches.

3.1.2 Improved results

Fig. 24 shows the standard deviation s of 8 average values for the TP and FP images. The number of TP and FP images were 72 and 76, respectively. Note that the standard deviations s for TP images are relatively small as expected for circle-like shapes, whereas the deviations for FP images are relatively large or widely distributed from large to small. Thus, after the discrimination by the variation along body axis and orientation features proposed in section 2, the TP and FP images can further be distinguished by the new feature s . In fact, FP=8% under the condition TP=90% when the algorithm classifies the images with $s > 0.01$ into non-nodules. In other words, FP decreased from 20% to 8% under the condition TP=90%.

Although the improvement achieved by the new feature is a good result, what we would like to stress here is that the combination of several effective features and classification techniques might be the most important for developing clinically useful CAD systems. The methods and the promising results presented in this paper may support the importance of the combination.

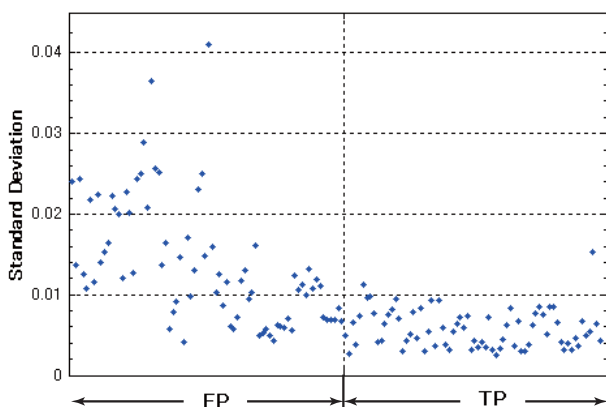


Figure 24: The standard deviation s of M average values for TP and FP images. s for TP images are relatively small as expected for circle-like shapes.

4 Conclusions

In this paper, we have proposed a new method to detect pulmonary nodules in X-ray CT images. From results in this study, we may claim that the proposed orientation and variation features of nodules can be useful for the pulmonary nodule diagnosis. The proposed method is based on the radiologist's diagnosis process. That is, by using the variation feature of shadows in the direction along the body axis, the method first selects nodule candidates and then only for the candidates, instead of all the images, the method further discriminates nodules from non-nodules by using the orientation feature details of shadow shapes. The selection can thus contribute to less computational expense.

Acknowledgements: This work was partially supported by The Ministry of Education, Culture, Sports, Science and Technology under Grant-in-Aid for Scientific Research #19500413, Kurokawa Cancer Research Foundation and Okawa Foundation for Information and Telecommunications.

References:

- [1] T. Iinuma, Y. Tateno, T. Matsumoto et al., "Preliminary specification of X-ray CT for lung cancer screening (LSCT) and its evaluation on risk-cost-effectiveness," *Nippon Acta Radiologica*, Vol. 52, pp. 182-190, 1992 (in Japanese).
- [2] T. Naruke, T. Goya, R. Tsuchiya, et al., "Prognosis and survival in resected lung carcinoma based on the new international staging system," *J. Thorac Cardiovasc Surg*, Vol. 96, pp. 440-447, 1988.
- [3] M. Prokop and M. Galanski, *Spiral and Multislice Computed Tomography of the Body*, Thieme Medical Publishers, Stuttgart, 2003.
- [4] International Early Lung Cancer Action Program (I-ELCAP) : Survival of Patients with Stage I Lung Cancer Detected on CT Screening, *NEJM*, Vol. 355, No. 17, pp. 1763-1771, 2006.
- [5] T. Okumura, T. Miwa, J. Kako, S. Yamamoto, M. Matsumoto, Y. Tateno, T. Iinuma and T. Matsumoto, "Variable-N-Quoit filter applied for automatic detection of lung cancer by X-ray CT," *Proc. of Computer-Assisted Radiology*, pp. 242-247, 1998 (in Japanese).
- [6] Y. Lee, T. Hara, H. Fujita, S. Itoh and T. Ishigaki, "Nodule detection on chest helical CT scans by using a genetic algorithm," *Proc. of*

IASTED International Conference on Intelligent Information Systems, pp. 67-70, 1997.

- [7] K. Suzuki, S. G. Armato, F. Le, S. Sone and K. Doi, "Massive training artificial neural network (MTANN) for reduction of false-positives in computerized detection of lung nodules in lowdose computed tomography," *Med.Phys.*, Vol. 30, No. 7, pp. 1602-1617, 2003.
- [8] Y. Nakamura, G. Fukano, H. Takizawa, S. Mizuno, S. Yamamoto, T. Matsumoto, S. Sone. F. Takayama. M. Koyama, S. Wada, "Recognition of X-ray CT image using subspace method considering translation and rotation of pulmonary nodules," *TECHNICAL REPORT OF IEICE*, Vol. 104, No. 580, MI2004-102, pp. 119-124, 2005 (in Japanese).
- [9] H. Takizawa, S. Kamano, S. Yamamoto, et al., "Quantitative analysis of cancer candidate regions in chest X-ray CT images," *J. Computer Aided Diagnosis of Medical Images*, Vol. 5, No. 2, pp. 4-11, 2001 (in Japanese).
- [10] RM. Haralick, et al., "Image Analysis Using Mathematical Morphology," *IEEE Trans. Pattern Analysis and Machine Intelligence*, Vol. 9, No. 4, pp. 532-550, 1987.
- [11] M. Nakayama, T. Tomita, S. Yamamoto, et al., "Study of 3D Morphological Filtering Applied for Automatic Detection of Lung Cancer X-ray CT," *Medical Imaging Technology*, Vol. 13, No. 2, pp. 155-164, 1995 (in Japanese).
- [12] M. Kondo, Y. Hirano, J. Hasegawa, J. Toriwaki, H. Ohmatsu, and K. Eguchi, "Classification of tumors in chest X-ray CT images into the solid and air-containing type and application to discrimination of the benign and malignant tumors," *TECHNICAL REPORT OF IEICE*, Vol.100, No.46, MI2000-16, pp. 27-32, 2000 (in Japanese).
- [13] C. W. Ngo, T. C. Pong, H. J. Zhang, "On clustering and retrieval of video shots through temporal slice analysis," *IEEE Trans. Mlt.*, Vol. 4, No. 4, pp. 446-458, 2002.
- [14] National Cancer Imaging Archive (NCIA), <https://imaging.nci.nih.gov/ncia/faces/baseDef.tiles>